Solar Phys (2013) 282:221–238
DOI 10.1007/s11207-012-0143-1

Comparisons of CME Morphological Characteristics Derived from Five 3D Reconstruction Methods

L. Feng · B. Inhester · M. Mierla

Received: 21 March 2012 / Accepted: 18 September 2012 / Published online: 2 November 2012

Abstract We compare different methods to reconstruct three-dimensional (3D) coronal mass ejection (CME) morphology. The explored methods include geometric localisation, mask fitting, forward modelling, polarisation ratio, and local correlation tracking plus triangulation. These five methods are applied to the same CME event that occurred on 7 August 2010. Their corresponding results are presented and compared, especially in their propagation direction and spatial extent in 3D. We find that the mask fitting and geometric localisation methods produce consistent results. Reconstructions including three-view observations are more precise than reconstructions done with only two views. Compared to the forward modelling method, in which an *a priori* shape of the CME geometry is assumed, the mask fitting has more flexibility. The polarisation ratio method makes use of the Thomson scattering geometry. We find that spatially the 3D CME derived from the mask fitting lies mostly in the overlap region obtained with the polarisation method using data from STEREO. In addition, the mask fitting can help resolve the front/back ambiguity inherent in the polarisation ratio method. However, the local correlation tracking plus triangulation did not show consistent results with the other four methods. This method performed poorly, primarily because

L. Feng (✉)
Key Laboratory of Dark Matter and Space Astronomy, Purple Mountain Observatory, Chinese Academy of Sciences, 210008 Nanjing, China
e-mail: lfeng@pmo.ac.cn

L. Feng · B. Inhester
Max-Planck-Institut für Sonnensystemforschung, Max-Planck-Str.2, 37191 Katlenburg-Lindau, Germany

B. Inhester
e-mail: binhest@mps.mpg.de

M. Mierla
Institute of Geodynamics of the Romanian Academy, Jean-Louis Calderon 19-21, 020032 Bucharest-37, Romania
e-mail: marilena@geodin.ro

M. Mierla
Royal Observatory of Belgium, Avenue Circulaire 3, 1180 Brussels, Belgium

the two STEREO spacecraft had a large angular separation. Under these circumstances, it is difficult to identify points taken from independent images that correspond to the same physical feature. Excluding the local correlation tracking method, the latitude of the CME's centre of gravity derived from the other methods deviates within 1°, and the longitude differs within 19°.

Keywords Corona, structures · Coronal mass ejections, initiation and propagation

1. Introduction

Coronal mass ejections (CMEs), which are violent eruptions from the Sun, are known to be the main cause of major geomagnetic storms. They can now be observed from three viewpoints almost simultaneously using the two separated *Solar Terrestrial Relations Observatory* (STEREO; Kaiser *et al.*, 2008) spacecraft and the *Solar and Heliospheric Observatory* (SOHO; Domingo, Fleck, and Poland, 1995). COR1 and COR2 are white light coronagraphs in the *Sun Earth Connection Coronal and Heliospheric Investigation* (SECCHI; Howard *et al.*, 2008) instrument package onboard STEREO. *Large Angle and Spectroscopic Coronagraph* (LASCO; Brueckner *et al.*, 1995) C2 and C3 are white light coronagraphs onboard SOHO. They provide time-resolved polarised and total brightness images of eruptions in the corona. These measurements can be used to derive the location and three-dimensional (3D) structure of CMEs, which is crucial for understanding the origin and dynamics of these eruptions and for predicting their effects on the Earth's magnetosphere.

A number of methods have been developed to obtain the 3D morphology of CMEs from multi-view coronagraph data. Mierla *et al.* (2009, 2010) and Thernisien, Vourlidas, and Howard (2011) compared the results of different reconstruction methods. de Koning, Pizzo, and Biesecker (2009) calculated a stack of quadrilaterals which contain the 3D CME position and shape. Byrne *et al.* (2010) fitted an eclipse to the quadrilateral in an attempt to derive a smooth CME shape. A different approach to estimate the 3D CME morphology uses forward modelling assuming a graduated cylindrical shell flux rope model for the CME (Thernisien, Vourlidas, and Howard, 2009; Thernisien, 2011). This flux rope model is controlled by a few free parameters determined by fitting the flux rope with the observed CME from different viewpoints. Another method, the polarisation method, was first applied by Moran and Davila (2004). It makes use of the anisotropy of the differential Thomson scattering cross section for different polarisations of the scattered photon. This effect allows us to estimate a virtual centre of the scattered signal along each line of sight from the observed polarisation ratio.

Feng *et al.* (2012) developed a new mask fitting method to investigate the CME localisation and morphology. It has been used to determine the propagation direction of CMEs and interpret *in situ* observations from different viewpoints. The morphological evolution of the CME was analysed as well. The orientation of the neutral line in the source region was compared with the major direction of the reconstructed 3D cloud and the flux rope axis orientation from the *in situ* data. To validate the newly developed reconstruction method and to seek a reliable method for the purpose of space weather prediction, in this paper the mask fitting method is compared with a few other methods which have been used to reconstruct the 3D shape. In Section 2 the observations of a specific CME are presented. Different methods applied to the same CME event are introduced with their corresponding results in Section 3. In Section 4 we compare and combine the mask fitting method with the other four methods. The final section presents the discussion and conclusions.

Table 1 Longitude and latitude of STEREO-A/B and SOHO in the Carrington coordinate system.

Spacecraft	B	SOHO	A
Longitude	311.49	22.86	102.21
Latitude	−1.83	6.19	4.81
Separation with SOHO	71.61		79.01
Separation (A–B)		150.61	

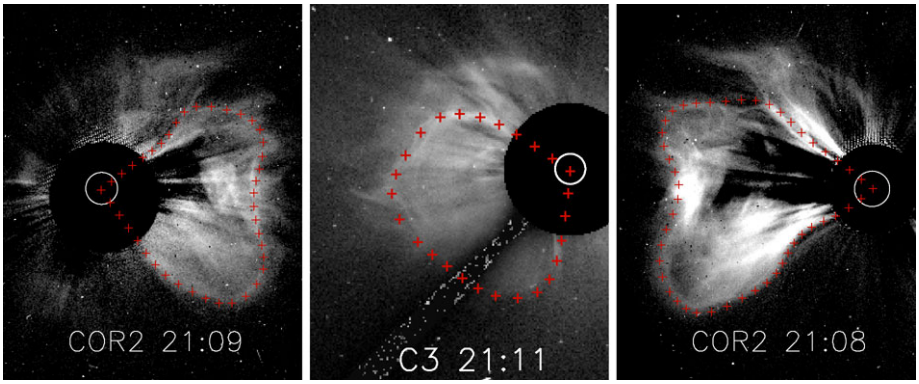

Figure 1 The coronagraph images recorded by STEREO-B/COR2 at 21:09:05, by SOHO/LASCO C3 at 21:11:18 and by STEREO-A/COR2 at 21:08:15 on 7 August 2010. The red curves outline the CME region traced by hand.

2. Observations and Data Reduction

The CME for which the 3D morphology is reconstructed was observed on 7 August 2010. Its propagation in interplanetary space can be traced in the field of view of COR and HI (*Heliospheric Imager*) in the SECCHI instrument package onboard STEREO. The CME of interest was also observed by LASCO C2 and C3 onboard SOHO. In this paper, the 3D CME cloud is reconstructed only from Sun-centred coronagraph images. We are not dealing with the data observed by HI at this stage. The data from SECCHI COR2 and LASCO C3 are used. More generally, the methods introduced in the following section can be applied to any other coronagraph data if it includes polarisation measurements.

SECCHI COR2 has a field of view extending from 2.5 to 15 $R_\odot$, whereas LASCO C3 has a larger field of view extending from 3.7 to 30 $R_\odot$. The spatial resolution of COR2 and C3 is 15 and 56 arcsec pixel^{-1}, respectively. COR2 and C3 both have a polariser which allows measurements of total, polarised and unpolarised brightness. The total time required for a polarimetric observation sequence for COR2 is around 20 s, while the corresponding observation using LASCO is around 300 s. The shorter exposure times eliminate errors arising from CME motion between exposures. All the processing of coronagraph images is done by secchi_prep and lasco_prep in SolarSoft (SSW). For a 3D reconstruction from images observed at two or three viewpoints, the positions of each spacecraft are required. In Table 1 we list the longitude and latitude of STEREO-A/B and SOHO in the Carrington coordinate system. The separation angles between the spacecraft are also shown.

In Figure 1 the background-subtracted coronagraph images are presented. In the following, SECCHI COR2 on STEREO-A and B will be designated as COR2-A and COR2-B for short, respectively. To make the CME signature more prominent, the background for

COR2 is a pre-CME image recorded about 40 min before the eruption. Its subtraction can remove the stray light and non-CME coronal emissions. The background for C3 is a computed 12-h minimal image centred at the time of the CME eruption. Such background subtraction mainly removes the stray light; the streamer is still visible. The CME periphery was traced by hand and fitted by a cubic spline. The CME-edge tie-points are indicated by red crosses for a time instance at around 21:10 UT. In our calculations we ignored the 3-min time difference between the observations of COR2-A/B and C3. We have considered the interpolation of the C3 CME from two neighbouring frames in time. However, we found that the observational time of one of the neighbouring frames was almost half an hour earlier. It is very probable that the error induced by the interpolation would exceed the error from the CME propagation in 3 min. In Figure 1 shock signatures were observed which are not included in the calculations below.

The most prominent activity on the solar disk occurred at the time of the CME launch in active region (AR) 11093 located at N12E31 as viewed from the Earth on 7 August. According to GOES light curves, an M-class flare occurred in this active region. It started around 17:55 UT and peaked at 18:24 UT. AR 11093 was visible in the east with respect to the central meridian as seen from the Earth observed by the *Atmospheric Imaging Assembly* (AIA; Lemen *et al.*, 2012) onboard the *Solar Dynamics Observatory* (SDO), whereas in the west it was observed by the *Extreme Ultraviolet Imager* (EUVI; Wuelser *et al.*, 2004) onboard STEREO-B. It was behind the solar limb as seen from STEREO-A. More details of the investigated CME and its source region can be found in Feng *et al.* (2012).

3. Descriptions and Results of Different 3D Reconstruction Methods

For direct comparisons of different reconstruction methods, all the calculations are done for the same CME event and in the same Cartesian Carrington coordinate system. For this right-handed coordinate system, the X- and Y-axes lie in the solar equatorial plane, with the X-axis pointing to zero Carrington longitude, and the Z-axis is the solar rotation axis.

3.1. Geometric Localisation (GL)

The geometric localisation method we use resembles the work in de Koning, Pizzo, and Biesecker (2009). The reconstruction is based on the epipolar geometry (Inhester, 2006). From two viewpoints of spacecraft 1 and 2 at positions $\mathbf{r}_1$ and $\mathbf{r}_2$, the epipolar reference axis is in the direction of $\mathbf{r}_1 \times \mathbf{r}_2$. For the stereoscopic reconstruction, all epipolar planes include the spacecraft positions $\mathbf{r}_1$ and $\mathbf{r}_2$. The epipolar plane which also includes the Sun centre is normal to the reference axis. If one certain epipolar plane is chosen, its intersection with two image planes yields two epipolar lines. In each image plane the intersection of the epipolar line with the projected CME surface produces two intersection points: one on the CME leading edge and the other on the rear edge. The back projections of these four points form one quadrilateral in each epipolar plane which contains the CME. The stacked set of quadrilaterals on different epipolar planes yields a volume which to a first approximation reconstructs the CME shape in 3D space.

As an example, we present in Figure 2 the reconstruction that resulted from only two views, COR2-B and LASCO/C3. Figure 2(a) is a view of the 3D CME from a vantage point above the north pole. From this particular viewpoint, the position of the 3D CME relative to the three view directions from STEREO-A/B and SOHO can be easily disentangled. For a low-latitude CME around the ecliptic plane, as is the case in this paper, this information is

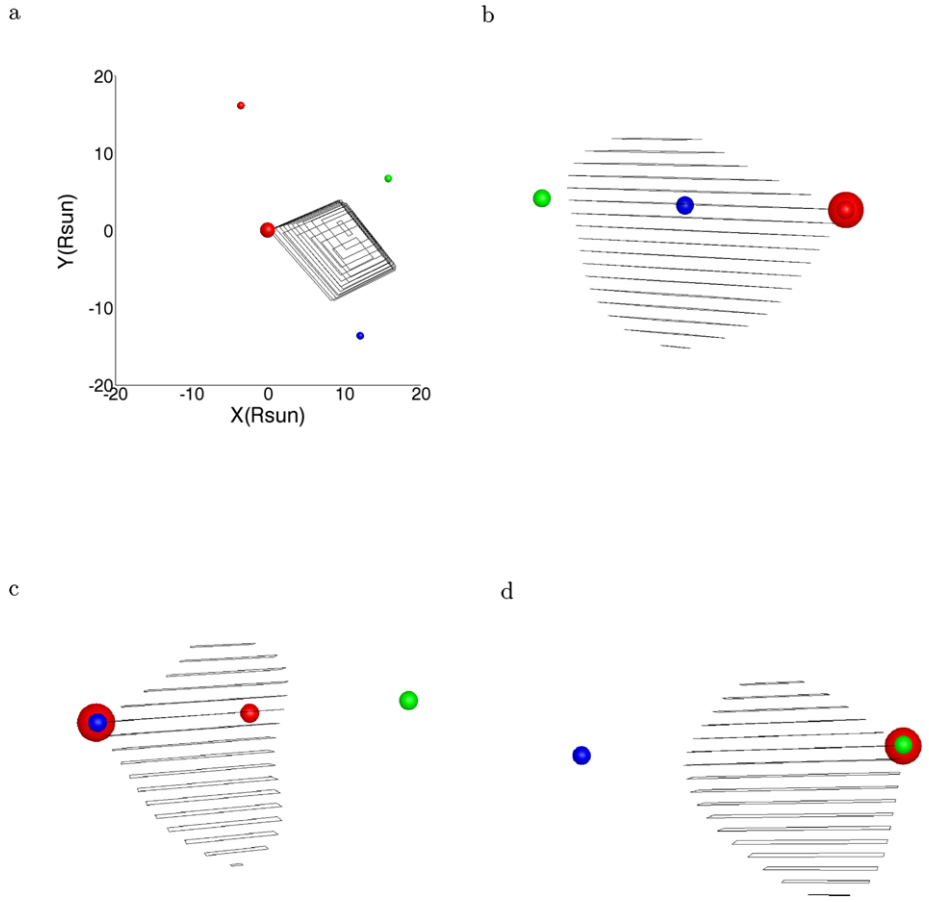

Figure 2 Reconstructed 3D CME from STEREO-B/COR2 and SOHO/LASCO C3. Panel (a) is a top view. The red sphere represents the position of the Sun. Three smaller spheres from top to bottom indicate the positions of STEREO-A (red), SOHO (green), and STEREO-B (blue), respectively. Their distances to the Sun are scaled down. Panels (b) through (d) are the reconstructed 3D CME as seen by STEREO-A, STEREO-B, and SOHO.

very helpful to tell whether a CME will arrive at the Earth or at another planet/spacecraft. A high-latitude CME may eventually deflect to the heliospheric current sheet close to the ecliptic plane where planets reside (see *e.g.* Zuccarello *et al.*, 2012; Shen *et al.*, 2011). Figures 2(b) – 2(d) are the projections of the reconstructed CME onto the image plane of STEREO-A/B and SOHO. They have very similar shapes to that of the CME observed by COR2-A and C3. However, the CME shape in panel (b) and in Figure 1 as seen from COR2-A do not fit each other exactly. Since the reconstruction only includes the CME periphery from COR2-B and C3, it is not surprising that we arrive at this result. The deviations reveal that observations from a third viewpoint will further constrain the CME shape.

In Figure 3, the red quadrilateral is the reconstruction from COR2-A and B in the epipolar plane across the solar centre. The green and blue quadrilaterals are similar to the red one, but constrained by COR2-A and C3, COR2-B and C3, respectively. Because the three spacecraft

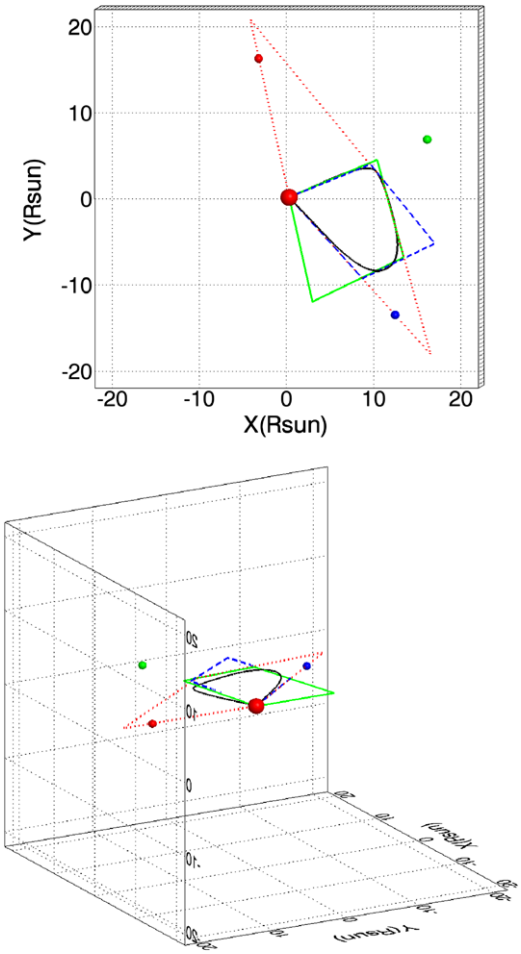

Figure 3 Geometric localisation of the CME in the epipolar plane containing the solar centre is shown by three parallelograms. The red dotted parallelogram is reconstructed from the coronagraphs observed by STEREO-A and B, the green solid one from STEREO-A and SOHO, and the blue dashed one from STEREO-B and SOHO. The black solid curve is the reconstruction in the solar equatorial plane with the mask fitting method. The red sphere represents the Sun. The three smaller spheres are STEREO-A, SOHO, and STEREO-B. The colour code of the three spacecraft is the same as in Figure 2. (Top) A top view of the reconstructions. (Bottom) A side view showing the small deviation of the epipolar planes from the equatorial plane.

were almost positioned in the same plane, these three epipolar planes (three quadrilaterals) determined by STEREO-A/B, SOHO, and the Sun are roughly coplanar.

It is obvious that the red quadrilateral extends in a much bigger range in longitude than the green and blue ones; that is, its corresponding uncertainty of reconstruction is much larger. Pizzo and Biesecker (2004) investigated the uncertainty of the 3D reconstructions with the geometric localisation technique as a function of the separation angle. Synthetic white light image pairs simulating STEREO-like coronagraph observation of a modelled 3D CME were created. The reconstructions from the synthetic image pair at different separation angles and the modelled 3D CME were compared. The ratio of the area of the reconstructed quadrilateral to the actual area was around unity at a 90° separation, and increased almost monotonically to both 0° and 180° separations. In Figure 3, the reconstruction in red has an area much larger than the green and blue ones due to the large separation angle between STEREO-A and B. This is consistent with the scenario depicted in Pizzo and Biesecker (2004).

Another immediate result which can be derived from Figure 3 is that the common polygon area which results from the intersection of the red, green and blue quadrilaterals is more constraining than any of the individual quadrilaterals from just two view directions. We

therefore strongly recommend that the third viewpoint should be included, if the data are available.

However, as mentioned at the beginning of this section, an epipolar plane depends on the position of the two observing spacecraft. If more than two spacecraft are used, epipolar planes still need to be constructed between each pair of spacecraft, and epipolar planes from different spacecraft pairs in general will not match. However, if three spacecraft are located in a common plane with the Sun centre, the various epipolar planes can be approximated by planes parallel to the common spacecraft plane. This is equivalent to assuming an affine instead of a projective viewing geometry. The error introduced is small ($O(r_{\mathrm{CME}}/r_{\mathrm{spacecraft}})$) as long as the CME is observed close to the Sun, where the distance r is measured from the Sun. If the three spacecraft do not lie in a common plane the reconstruction by geometric localisation is still possible, but more complicated, because it can no longer be reduced to a set of planar intersections. Instead the CME volume for each pair of spacecraft could be determined as a set of quadrilaterals on stacked epipolar planes, and the intersections would have to be calculated from these volumes as a whole rather than from the quadrilaterals in each (approximate) epipolar plane.

3.2. Mask Fitting (MF)

The mask fitting method geometrically follows up the previous concept; however, instead of performing back projections and finding intersections on epipolar planes, we use forward projections from a discretised 3D space to verify whether a 3D point is potentially inside or outside the CME volume. Using this concept, the epipolar geometry is not required explicitly. The details of this method are described in Feng *et al.* (2012).

As a first step, three CME masks are created according to Figure 1. The pixel value is one inside the CME periphery and zero outside. Then we discretise a 3D cube centred at the Sun and in the range from $-15R_{\odot}$ to $15R_{\odot}$ for all three coordinate axes. Each point in this 3D cube is projected onto three image planes of STEREO-A/B and SOHO, respectively. Only those points which are projected onto the masks of all three images are considered to be the 3D points belonging to the CME. Afterwards, Bézier curves are employed to smooth the boundary of the resulting polygonal volume. In Figure 3 the black curve shows a slice of the smoothed reconstructed CME volume in the solar equatorial plane $z = 0$.

The different views of the reconstructed 3D CME with the mask fitting method are shown in Figure 4. Compared with the results obtained by using epipolar geometry explicitly with STEREO-B/COR and SOHO/LASCO data, the reconstruction from three views provides a better solution, as verified by Figure 4(b). The heart-like shape along the CME leading edge as seen from STEREO-A is now clearly visible, whereas this feature is not present in Figure 2(b). In Figure 4(d) three principle axes and the geometric centre of the 3D CME volume are shown. Details of the computation can be found in Feng *et al.* (2012). Note that the geometric centre might not be the centre of gravity since a uniform density distribution was assumed. In this paper we use it as an approximation of the centre of gravity to make comparisons with other methods.

3.3. GCS Forward Modelling (FM)

Thernisien, Howard, and Vourlidas (2006) and Thernisien, Vourlidas, and Howard (2009) developed a forward modelling technique for flux-rope-like CMEs using an empirically defined model of a flux rope: the graduated cylindrical shell (GCS). It consists of a tubular section forming the main body of the structure attached to two cones that correspond to

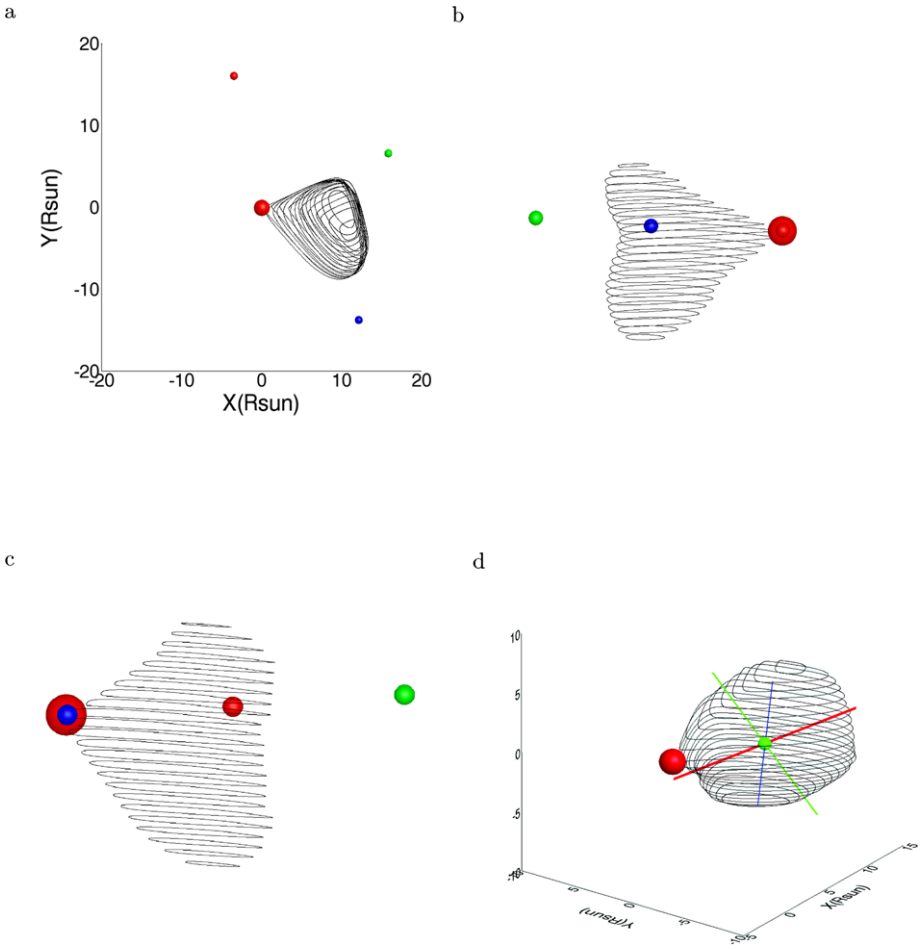

Figure 4 Reconstructed 3D CME with the mask fitting method from STEREO-B/COR2 and SOHO/LASCO C3. Panel (a) is a top view. The red sphere indicates the position of the Sun. The three smaller spheres are STEREO-A, SOHO, and STEREO-B. The colour code of the three spacecraft is the same as in Figure 2. Panels (b) and (c) are the reconstructed 3D CME as seen by STEREO-A and B. In panel (d) the 3D CME and its three principle axes are plotted. The three axes in red, green, and blue are the major, intermediate, and minor axes, respectively. The small green sphere represents the geometric centre of the CME.

the legs of the CMEs. The parameters constraining the shape of the flux rope are determined by visual comparison of the projected 3D flux rope to observations. The optimisation is achieved by trial and error. One hour after launch, the CME leading front became concavely deformed, and its shape could no longer match that of a single flux rope. Therefore, a flux rope does a poor job for this CME. However, as a first estimate of the 3D propagation direction and the spatial extension of the CME, in Figure 5 a flux rope is fitted to the observed CME from three viewpoints: STEREO-B, LASCO, and STEREO-A. We followed the proposal of Thernisien, Vourlidas, and Howard (2009) and fitted two flux ropes to the observations from three viewpoints. The results are presented in Figure 6 in blue together with a single flux rope in red for comparison.

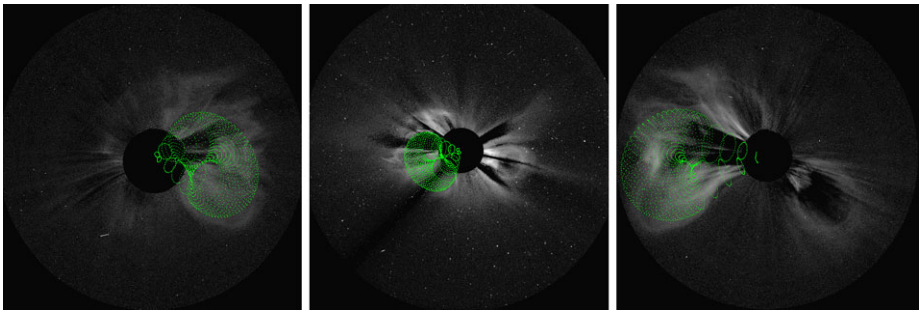

Figure 5 Fitting of a flux rope to the CME observed by COR2-A, C3, and COR2-B with the GCS forward modelling method.

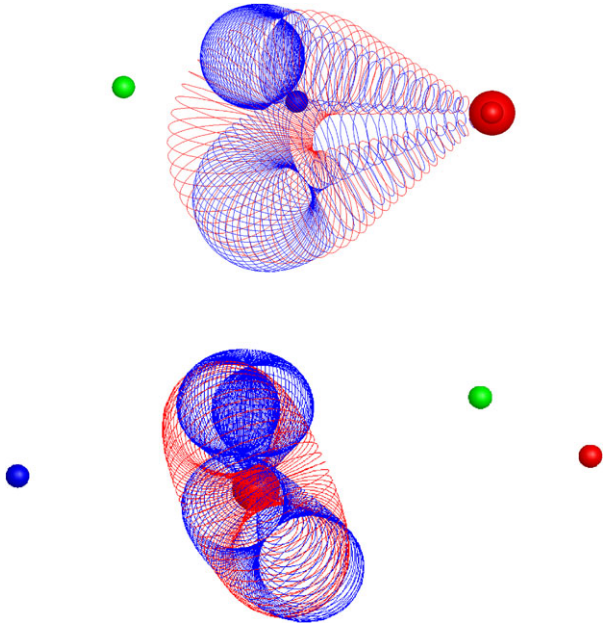

Figure 6 3D flux ropes with the best-fit parameters derived from the forward modelling method. The red flux rope represents a single flux rope fitted to the CME observed from three viewpoints. Two blue flux ropes are combined to fit to the observed CME. The red sphere stands for the Sun; the three smaller spheres indicate the directions to three spacecraft. The same colour code as in Figure 2 applies here to the three spacecraft. (Top) Flux ropes as seen from STEREO-A. (Bottom) Flux ropes as seen from the top of the fitted single flux rope.

3.4. Polarisation Ratio (PR) Technique

The polarisation ratio technique was first applied to SOHO/LASCO coronagraph images before the launch of STEREO (Moran and Davila, 2004; Dere, Wang, and Howard, 2005). Theoretically, the degree of polarisation of Thomson scattered light by electrons in the corona is a sensitive function of the scattering angle between the direction of the incident light and the direction towards the observer (Billings, 1966). Hence the ratio of the polarised brightness pB to the unpolarised brightness $tB - pB$, where tB is the total brightness, is also a function of the scattering angle. Equivalently, this angle can be converted to an effective distance of the scatterer from the plane of the sky (POS). Observationally, the polarisation ratio can be retrieved from the polarimetric observation sequence by LASCO or COR2 for each pixel within the CME region. Comparing with the theoretical relation, we can derive a weighted distance of the centre of scattering along the line of sight (LOS) for each pixel.

Mierla *et al.* (2009) applied this technique to several CMEs observed by COR-A and B independently, and derived the distribution of LOS scattering centres of the CME. Moran, Davila, and Thompson (2010) have validated this method through triangulation. de Koning and Pizzo (2011) have suggested that this method can be used in space weather forecasting.

To remove the contributions other than the CME feature itself (*i.e.* from the F-corona, stray light, and streamers), a pre-event image was subtracted. The emission in the coronagraph images is Thomson scattered light, but in some situations Hα emission can also be observed (see *e.g.* Mierla *et al.*, 2011). We assumed that only Thomson scattered light was observed; thus we could use the PR method to derive the 3D location of the CME. In order to increase the signal-to-noise ratio, the frames with the CME were smoothed by using a 5 by 5-pixel median filter. The size along the LOS is restricted to 15 $R_{\odot}$ (in front and behind the POS), and the step size along the LOS is every 0.001 $R_{\odot}$. In order to reduce artefacts in the 3D reconstruction, the pixels where the intensity was smaller than 5 % of the mean value over the CME region were not included in the calculation.

Figure 7 shows the results of applying the PR method to the data of COR2-A (PR-A method) and B (PR-B method) on the left and right panels, respectively. The colour bar indicates the distances in solar radii of the scattering centres off the POS obtained for each image pixel inside the CME projection. The bottom panel is a top view of the reconstructed 3D points. Yellow and green points represent the results from COR2-A and B, respectively. As the PR method can only determine an absolute distance to the POS, an ambiguity of two symmetric solutions arises. When the CME source region is known, its position in the solar disk can be utilised as a reference. From the proximity in the times of flare eruption and CME ejection, the source region is probably AR 11093. It was located on the western hemisphere as seen from STEREO-B. From STEREO-A, it was not visible in front of the solar limb. Therefore, we assume that all the reconstructed points from the PR method are behind the POS as seen from STEREO-A, whereas they are in front of the POS as seen from STEREO-B.

The results from COR2-A and B in Figure 7 are generally consistent with each other. In the top view (bottom panel), a substantial part of the yellow and green points overlap. However, the misalignment is also obvious. The longitude of the centre of gravity differs by 19.4°. In addition, the reconstruction from COR2-B in the top panels indicates that the southern part has a larger distance to the POS than the northern part, while the reconstruction from COR2-A does not show this trend. We partly attributed the misalignment to the fact that some features can only be seen by one instrument. Also, in the above reconstructions, we assumed that the CME is fully behind the solar limb as seen from STEREO-A and fully in front of the solar limb as seen from STEREO-B. In reality, this may not be true for all pixels.

We note that two symmetric solutions exist for one pixel: one in front of the POS and the other behind. This ambiguity can be partly disentangled by the identification of the source region in EUV images or by the best match of stereoscopic observations. However, CME source regions are not always apparent, *e.g.*, for stealth CMEs (Robbrecht, Patsourakos, and Vourlidas, 2009). Furthermore, without the information of the density distribution along the LOS, the determined distance to the POS might contain some errors (Mierla *et al.*, 2009), even if we include the stereoscopic results. A further source of error of the polarisation ratio method may be that low temperature chromospheric material might enter the coronagraph field of view whose radiation mechanism is totally different from the Thomson scattering. Therefore, in those cases the polarisation ratio technique does not work properly (Mierla *et al.*, 2011).

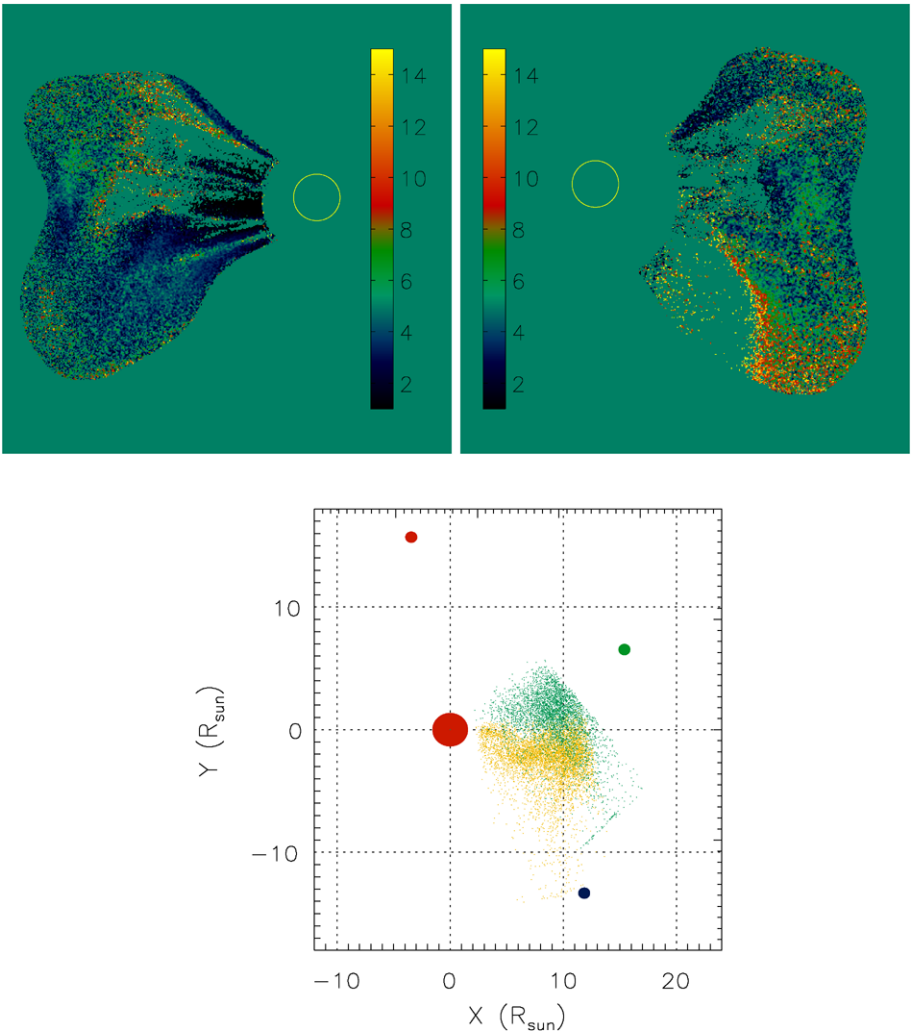

Figure 7 Reconstructed 3D points from the polarisation ratio method. (Top) The weighted distance of each pixel in the CME region to the respective POS calculated from COR2-A (left) and COR2-B (right). The colour bar scales the distance in solar radii. The yellow circles mark the position of the solar disk. (Bottom) A top view of the reconstructed 3D points. To make the dot density visible, we plotted the scattering centre every 50 points for all the 3D points. The yellow points are from the reconstruction from COR2-A, the green points from COR2-B. The red sphere indicates the Sun, and the three smaller ones mark the directions to the three spacecraft. The colour code of the three spacecraft is the same as in Figure 2.

3.5. Local Correlation Tracking Plus Triangulation (LCT-TR)

A crucial step in this approach is to correlate the CME texture in both images before the triangulation. Since a CME often appears as a diffuse cloud, instead of the feature-based approach Mierla *et al.* (2009) applied a local correlation tracking (LCT) method to find the corresponding points in a STEREO image pair. Following the same method, we have first co-aligned the images in the STEREO mission plane such that the epipolar lines become

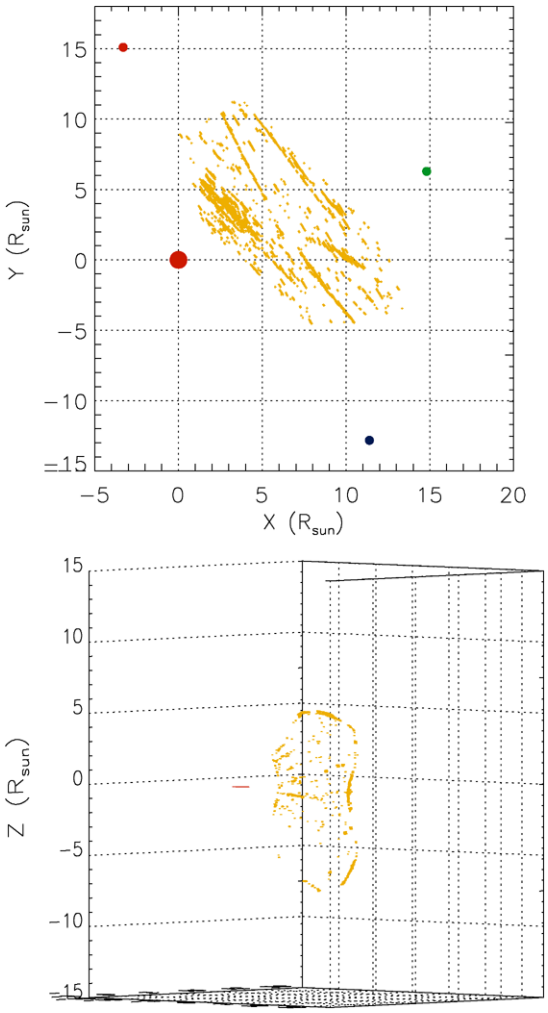

Figure 8 (Top) A top view of the reconstruction with the LCT-TR method from COR2-A and B. The four spheres have the same meaning as in Figure 7. (Bottom) A view from STEREO-B. In both panels, the lower limit of the correlation coefficient is set to 0.7 for the correspondence.

nearly horizontal. The elements to be matched are small subimages of a fixed size, called match windows. The criterion which decides whether two such windows in different images are positioned on the same object is the magnitude of their mutual correlation coefficient. The cross-correlation is calculated from windows on two STEREO images on a common epipolar line. For a given position of one window on the epipolar line in one image, the corresponding position of the matching window in the other image is determined by the correlation maximum.

Once the correspondence between pixels is established, the point in 3D space is calculated through back projection (Inhester, 2006). In Figure 8, we present the LCT-TR reconstruction of the CME from COR2 data. A threshold of acceptance for the calculated correlation minimum of 0.7 was used in Figure 8. In order to find correlations in two images, the match window (11 × 11 pixels) was fixed in a position on a given epipolar line in one image and we moved it along the same epipolar line in the other image. The search window was 512 pixels in the horizontal direction.

As the CME was observed at the opposite limb in the two images, the search for corresponding features was flipped such that, for a pixel on the left side of image A, the search window was located on the right side of image B. The upper panel of Figure 8 is a top view. The reconstructed CME shows a propagation direction towards SOHO which was, however, not validated by the *in situ* observation close to the Earth (Feng *et al.*, 2012). It may be that the lower acceptance limit of 0.7 for the correlation was chosen too small, causing a significant number of false correlations to be passed. However, a higher value of the correlation limit would have markedly reduced the number of correlations. The lower panel of Figure 8 is a view from STEREO-B. Most of the points within the CME periphery have a correlation coefficient of less than 0.7. The results of LCT-TR clearly show a poor performance when the separation angle of the two STEREO spacecraft is large.

4. Comparison and Combination of Different Methods

4.1. Geometric Localisation and Mask Fitting

The reconstruction of the CME morphology is a typical inverse problem. The geometric localisation method uses back projection to find a solution, whereas we use forward projections in the mask fitting algorithm. In Figure 3, we can see that the black curve from the mask fitting method fits the pentagon from the geometric localisation quite well. The small difference between the mask fitting and geometric localisation methods is that the epipolar plane does not necessarily lie on the solar equatorial plane of $z = 0$. They deviate from each other by a few degrees, as indicated in the bottom panel of Figure 3. Nevertheless, from Figure 3, in principle these two methods should produce consistent results.

The geometric localisation suffers from the limitation that the epipolar plane is uniquely determined by the positions of the two spacecraft and the point to be reconstructed. Only in the rare case that the third spacecraft also lies in this epipolar plane can we combine the constraints from the three viewpoints in a simple way. However, the mask fitting method can integrate the data from an unlimited number of viewpoints with arbitrary positions. Obviously, the more view positions that are included in the reconstructions, the more constrained and reliable is the result.

4.2. GCS Forward Modelling and Mask Fitting

As stated in Section 3.3, when a CME does not have the shape of a flux rope, the GCS forward modelling method can only provide an approximation of the 3D CME morphology. A common feature of any forward modelling is that the result strongly depends on an *a priori* geometrical assumption. However, real CMEs do not always have a closely flux-rope-like shape. Therefore, we found that the mask fitting method has more flexibility than the forward modelling method. In the left panel of Figure 9, the fitted flux rope and the 3D CME reconstructed from the mask fitting method are shown superposed along a view direction which is perpendicular to the plane of the flux rope skeleton. We can see how much the single idealised flux rope may deviate from the true CME.

Both the orientation of the flux rope characterised by the tilt angle γ in Thernisien, Howard, and Vourlidas (2006) and the major principle axis from the mask fitting method are in the NE-SW direction, as seen in the right panel of Figure 9. The projected difference in direction between the major principle axis and the tilt angle derived from the GCS model is about 30 degrees.

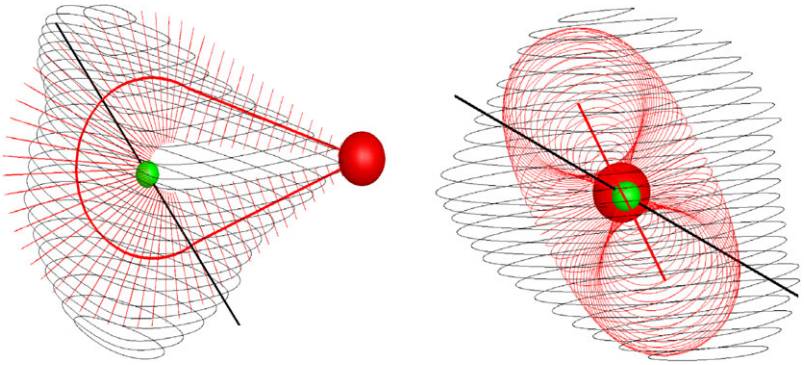

Figure 9 Comparison of the single flux rope from the forward modelling in red with the results from the mask fitting method in black. The red sphere is the Sun. The red curve is the CME skeleton from the GCS model. The black straight line indicates the major principle axis of the 3D CME cloud derived with the mask fitting method. The front view of the flux rope is presented in the left panel. The top view of the flux rope is in the right panel.

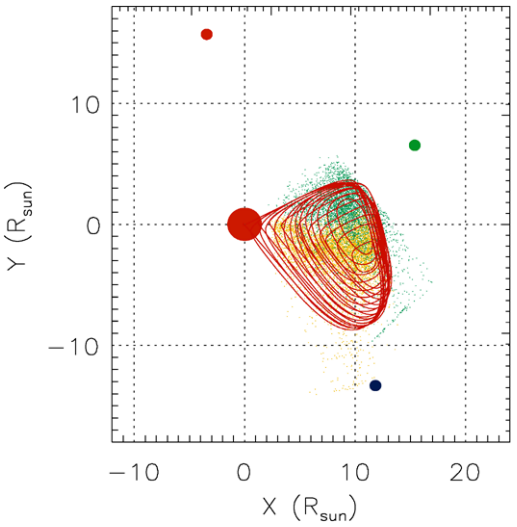

Figure 10 The top view of the 3D CME reconstructed with the MF technique (red), and with the PR method from COR2-A and B (yellow and green), respectively.

4.3. Polarisation Ratio and Mask Fitting

The polarisation ratio (PR) method has the advantage that only the data from one viewpoint and some additional information like the location of the CME source region are required for a unique reconstruction. It also yields some limited information about the interior structure of the CME. However, the polarisation ratio can only provide the depth of a virtual scattering centre for each LOS, not the depth range over which the CME extends along the LOS. Figure 10 shows the reconstructions with the PR and mask fitting (MF) methods superposed. Apparently, the MF method locates the CME mostly in the overlap region of the results with the PR method from the COR2-A and B images.

There was an ambiguity of the two symmetric solutions from the PR method in Section 3.4; we have resolved this ambiguity by reference to the location of the CME source

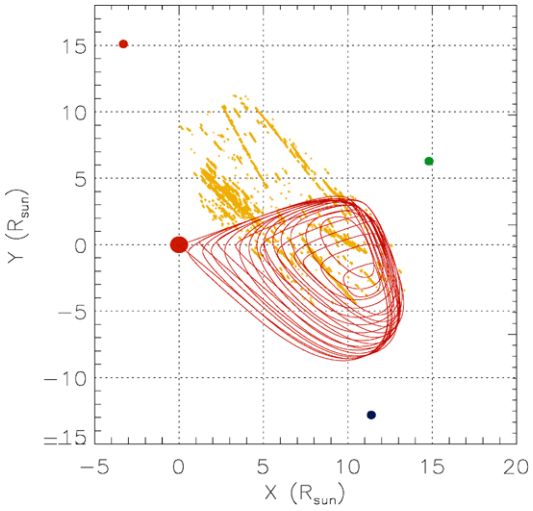

Figure 11 Comparison of the 3D CME reconstructed from the MF and LCT-TR methods. The results are shown in red and yellow, respectively.

region. If knowledge of the source region is not available, the CME shape reconstructed with the MF method could also be used as reference. For the CME studied here, the MF result suggests that the CME centre is completely in front of the POS as seen from STEREO-B and behind the POS for most pixels of STEREO-A. We therefore selected this respective solution for the PR method. Note that there is some probability of the LOS from STEREO-A passing close to the Sun, so that the PR scattering centre lies in front of the respective POS. Since the MF method gives only the shape but no density distribution inside the CME volume, predictions about the scattering centre must be treated with care if the MF volume extends to both sides of the POS. We also found that the centres of gravity obtained with MF and PR-A are quite close. However, those derived from MF and PR-B differ by more than one solar radius. Similarly, de Koning and Pizzo (2011) combined the 3D CME reconstructed with the geometric localisation method from two viewpoints to resolve the PR ambiguity.

4.4. Local Correlation Tracking plus Triangulation and Mask Fitting

The LCT-TR method works well for small separation angles (Mierla *et al.*, 2009), but when the separation angle increases, the capability of LCT to solve the correspondence problem decreases. Figure 11 presents a top view of the reconstructed CME with the MF (red) and LCT-TR methods (yellow). We found a large discrepancy between them. The 3D CME location derived from the LCT-TR method indicates a propagation of the CME towards the Earth, whereas the CME position obtained with the MF method is consistent with a propagation towards Venus (Feng *et al.*, 2012). As pointed out in Section 3.5, the *in situ* measurements around the Earth did not detect any ICME-related signature. However, the *Venus Express* spacecraft detected the shock and ICME arrival (Feng *et al.*, 2012). Therefore, we take this as evidence that the MF method for large spacecraft separation angles yields a more reliable 3D reconstruction than the LCT-TR method. The LCT-TR method appears to fit quite nicely inside the red quadrilateral obtained from the geometric localisation. In other words, LCT-TR suffers from the same large-angle separation problem that two-spacecraft geometric localisation does.

Table 2 Longitude and latitude of the centre of gravity, and longitude and latitude ranges of the reconstructed 3D CME obtained with the mask fitting (MF)/geometric localisation (GL), forward modelling (FM), polarisation ratio (PR-A/B), and local correlation tracking plus triangulation (LCT-TR) methods. The Carrington coordinate system is used. All values are in units of degrees.

Method	Lon.	Lat.	Lon. min	Lon. max	Lat. min	Lat. max
MF/GL	−13.3	−7.7	−48.0	24.7	−42.5	25.3
FM[a]	−13.4	−7.3	−35.6	11.0	−42.0	27.6
PR-A	−14.6	−7.9	−70.3	15.6	−42.1	39.1
PR-B	4.8	−6.8	−40.3	41.7	−55.6	42.8
LCT-TR	27.8	2.8	−29.7	89.4	−39.2	39.2

[a]Derived from the fit of a single flux rope.

5. Discussion and Conclusions

In this study we comprehensively compared the reconstruction results of five different methods which can produce the morphological shape of a 3D CME. The corresponding results and their comparisons with the newly developed mask fitting method (MF) are presented as well. For a quantitative comparison, we compiled in Table 2 the centre of gravity of the various 3D reconstructions and their range in longitude and latitude. Columns 4 – 7 of the table list the maximum and minimum longitude and latitude of the reconstructed 3D CME points.

For the geometric localisation method, we found in Section 4.1 that its result is consistent with the results obtained with the MF method. Therefore, we present the longitude and latitude information for both methods in the same row of Table 2. For the forward modelling method, the centre of gravity is obtained by assuming that the mass distribution has the same formula as in Thernisien, Howard, and Vourlidas (2006). As it is a symmetric distribution, we expect that the centre of gravity lies in the axis of symmetry of the modelled flux rope. Hence the centre of gravity has the same longitude and latitude as the central position of the source region. We found that the numerically calculated widths in latitude and longitude of the fitted flux rope model are consistent with the values analytically given by Equations (1) and (2) in Rodriguez *et al.* (2011). For a single GCS flux rope, the analytical formula gives a longitude range of about 45° and a latitude range of about 69°. From Table 2, these two figures, which were calculated numerically, are 46.6° and 69.6°, respectively.

An inspection of the longitude and latitude of the centre of gravity indicates that MF/GL, FM, and PR-A result in similar values. The difference in longitude is not greater than 1.3°, and in latitude is within 0.6°. PR-B shows a similar latitude. However, the longitude deviates by about 19°. Even larger deviations from those of the MF/GL methods were obtained with the LCT-TR method, both in longitude and latitude.

Concerning the spatial extension of the CME in 3D, the results in Table 2 are not fully consistent with each other. For the FM method, a single flux rope inclined in the NE-SW direction is fitted to coronagraph images observed from three viewpoints. As mentioned in Section 3.3, the observed CME was strongly deformed away from a simple flux rope. It is not surprising that the FM method has a different longitude and latitude extension than the MF method. Compared with the MF method, we found a smaller longitude range for the FM results. The latitude range derived from both methods agrees well. Interestingly, the longitude range from the MF method is generally consistent with the range of the overlap of the PR-A and PR-B results. There is a similar trend for the latitude minimum. However, the

latitude maximum obtained with the PR methods is 14° higher. The longitude and latitude range derived from the LCT-TR method shows a much bigger deviation from the other four methods. For large separation angle, the LCT-TR method does a poor job for the 3D reconstruction of CMEs.

In summary, for the event on 7 August 2010, we found that the MF method achieves the same precision for the CME's 3D morphology as the geometric localisation method when data from the same number of viewpoints are used. Compared with the forward modelling method, the MF method is more flexible, because no *a priori* geometrical assumption is required. We found that the MF method can be utilised to remove the ambiguity in the polarisation ratio method. In addition, the CME reconstructed with the MF method is located almost in the overlap region derived with the polarisation ratio method using COR2-A and B data. We did not find a consistent result of the local correlation tracking plus triangulation with the other four methods.

In general, the MF method produces a good 3D reconstruction of the CME surface if data from three spacecraft with sufficient angular separation are used. However, we are lacking a detailed internal structure within the CME volume. In the future, we will explore the MF method for the surface reconstruction in combination with tomography to resolve the internal density distribution. The localisation of the CME relative to the plane of the sky is helpful in estimating the CME mass from coronagraph images (see, *e.g.*, Colaninno and Vourlidas, 2009). It can be compared to the mass calculation from other observations (*e.g.*, Aschwanden *et al.*, 2009; Tian *et al.*, 2012). We anticipate that the information of the known propagation direction, spatial extension, and density distribution of a CME will allow more precise predictions of space weather.

Acknowledgements We thank S. Gissot for providing the LCT program. STEREO is a project of NASA. The SECCHI data used here were produced by an international consortium of the Naval Research Laboratory (USA), the Lockheed Martin Solar and Astrophysics Laboratory (USA), NASA Goddard Space Flight Center (USA), Rutherford Appleton Laboratory (UK), University of Birmingham (UK), Max Planck Institute for Solar System Research (MPS, Germany), Centre Spatiale de Liège (Belgium), Institut d'Optique Théorique et Appliqueé (France), and Institut d'Astrophysique Spatiale (France). LF is supported by the NSFC under Grants 11003047 and 11233008, by MSTC Program 2011CB811402, and by Grant BK2012889. LF also acknowledges the Key Laboratory of Dark Matter and Space Astronomy, CAS, for financial support. The contribution of BI benefited from the support of the German Space Agency DLR and the German Ministry of Economy and Technology under contract 50 OC 0904. MM thanks the MPS for financial support. Part of her work was also supported by the project TE 73/11.08.2010. The work at the MPS was supported by DLR contract 50 OC 0904.

References

Aschwanden, M.J., Nitta, N.V., Wuelser, J.-P., Lemen, J.R., Sandman, A., Vourlidas, A., Colaninno, R.C.: 2009, *Astrophys. J.* **706**, 376.

Billings, D.E.: 1966, *A Guide to the Solar Corona*, Academic Press, New York, 150.

Brueckner, G.E., Howard, R.A., Koomen, M.J., Korendyke, C.M., Michels, D.J., Moses, J.D., *et al.*: 1995, *Solar Phys.* **162**, 357.

Byrne, J.P., Maloney, S.A., McAteer, R.T.J., Refojo, J.M., Gallagher, P.T.: 2010, *Nat. Commun.* **1**.

Colaninno, R.C., Vourlidas, A.: 2009, *Astrophys. J.* **698**, 852.

de Koning, C.A., Pizzo, V.J., Biesecker, D.A.: 2009, *Solar Phys.* **256**, 167.

de Koning, C.A., Pizzo, V.J.: 2011, *Space Weather* **9**, 3001.

Dere, K.P., Wang, D., Howard, R.: 2005, *Astrophys. J. Lett.* **620**, L119.

Domingo, V., Fleck, B., Poland, A.I.: 1995, *Solar Phys.* **162**, 1.

Feng, L., Inhester, B., Wei, Y., Gan, W.Q., Zhang, T.L., Wang, M.Y.: 2012, *Astrophys. J.* **751**, 18.

Howard, R.A., Moses, J.D., Vourlidas, A., Newmark, J.S., Socker, D.G., Plunkett, S.P., *et al.*: 2008, *Space Sci. Rev.* **136**, 67.

Inhester, B.: 2006, arXiv:astro-ph/0612649.
Kaiser, M.L., Kucera, T.A., Davila, J.M., St. Cyr, O.C., Guhathakurta, M., Christian, E.: 2008, *Space Sci. Rev.* **136**, 5.
Lemen, J.R., Title, A.M., Akin, D.J., Boerner, P.F., Chou, C., Drake, J.F., *et al.*: 2012, *Solar Phys.* **275**, 17.
Mierla, M., Inhester, B., Marqué, C., Rodriguez, L., Gissot, S., Zhukov, A.N., Berghmans, D., Davila, J.: 2009, *Solar Phys.* **259**, 123.
Mierla, M., Inhester, B., Antunes, A., Boursier, Y., Byrne, J.P., Colaninno, R., *et al.*: 2010, *Ann. Geophys.* **28**, 203.
Mierla, M., Chifu, I., Inhester, B., Rodriguez, L., Zhukov, A.: 2011, *Astron. Astrophys.* **530**, L1.
Moran, T.G., Davila, J.M.: 2004, *Science* **305**, 66.
Moran, T.G., Davila, J.M., Thompson, W.T.: 2010, *Astrophys. J.* **712**, 453.
Pizzo, V.J., Biesecker, D.A.: 2004, *Geophys. Res. Lett.* **31**, 21802.
Robbrecht, E., Patsourakos, S., Vourlidas, A.: 2009, *Astrophys. J.* **701**, 283.
Rodriguez, L., Mierla, M., Zhukov, A.N., West, M., Kilpua, E.: 2011, *Solar Phys.* **270**, 561.
Shen, C., Wang, Y., Gui, B., Ye, P., Wang, S.: 2011, *Solar Phys.* **269**, 389.
Thernisien, A.: 2011, *Astrophys. J. Suppl.* **194**, 33.
Thernisien, A.F.R., Howard, R.A., Vourlidas, A.: 2006, *Astrophys. J.* **652**, 763.
Thernisien, A., Vourlidas, A., Howard, R.A.: 2009, *Solar Phys.* **256**, 111.
Thernisien, A., Vourlidas, A., Howard, R.A.: 2011, *J. Atmos. Solar-Terr. Phys.* **73**, 1156.
Tian, H., McIntosh, S.W., Xia, L., He, J., Wang, X.: 2012, *Astrophys. J.* **748**, 106.
Wuelser, J.-P., Lemen, J.R., Tarbell, T.D., Wolfson, C.J., Cannon, J.C., Carpenter, B.A., *et al.*: 2004, In: Fineschi, S., Gummin, M.A. (eds.) *Telescopes and Instrumentation for Solar Astrophysics, Proc. SPIE* **5171**, 111.
Zuccarello, F.P., Bemporad, A., Jacobs, C., Mierla, M., Poedts, S., Zuccarello, F.: 2012, *Astrophys. J.* **744**, 66.